

## Velocities and Temperatures of an Ellerman Bomb and Its Associated Features

Heesu Yang · Jongchul Chae · Eun-Kyung Lim ·  
Hyungmin Park · Kyuhyoun Cho · Ram Ajor Maurya ·  
Donguk Song · Yeon-Han Kim · Philip R. Goode

Received: 28 December 2012 / Accepted: 21 June 2013 / Published online: 26 July 2013  
© Springer Science+Business Media Dordrecht 2013

**Abstract** We investigated the velocity and temperature characteristics of an Ellerman bomb (EB) and its associated features based on observations made with the Fast Imaging Solar Spectrograph (FISS) and a broadband TiO filter of the 1.6 meter New Solar Telescope at Big Bear Solar Observatory. In the TiO images of the photospheric level, we found a granular cell expanding in two opposite directions near the site of the EB. When one end of this granule reached the EB site, the transverse speed of the tip of the expanding granule rapidly decreased and the EB brightened. The wings of the H $\alpha$  profile of the EB indicated that the EB was blueshifted up to 7 km s<sup>-1</sup>. About 260 s after the EB brightening, a surge was seen in absorption and varied from a blueshift of 20 km s<sup>-1</sup> to a redshift of 40 km s<sup>-1</sup> seen in the H $\alpha$  and Ca II 8542 Å lines. From the Doppler absorption width of the two lines determined by applying the cloud model, we estimated the mean temperature of the surge material to be about 29000 K and the mean speed of nonthermal motion to be about 11 km s<sup>-1</sup>. We discuss the physical implications of our results in terms of magnetic reconnection and processes related to it.

**Keywords** Active regions, velocity field · Chromosphere, active · Magnetic reconnection, observational signatures · Spectrum, visible · Velocity fields, photosphere

---

Initial Results from FISS  
Guest Editor: Jongchul Chae

---

H. Yang (✉) · J. Chae · H. Park · K. Cho · R.A. Maurya · D. Song  
Astronomy Program, Department of Physics and Astronomy, Seoul National University, Seoul 151-747,  
Korea  
e-mail: [yang@astro.snu.ac.kr](mailto:yang@astro.snu.ac.kr)

J. Chae  
e-mail: [chae@astro.snu.ac.kr](mailto:chae@astro.snu.ac.kr)

E.-K. Lim · Y.-H. Kim  
Korea Astronomy & Space Science Institute, Daejeon 305-348, Korea

P.R. Goode  
Big Bear Solar Observatory, Big Bear City, CA 92314-9672, USA

## 1. Introduction

An Ellerman bomb (EB) is a small feature in an active region that appears bright at the far wings of the  $H\alpha$  line (Ellerman, 1917). It has a short lifetime of about 10 min, and a size of about  $1''$  (Kurokawa *et al.*, 1982). It frequently occurs in an emerging flux region or near a sunspot. It usually has internal mass motions that often accompany a surge (Georgoulis *et al.*, 2002).

At the site of EBs, two types of internal mass motions were reported so far: downflows in the photosphere and upflows in the low chromosphere. Georgoulis *et al.* (2002) found that 80 % of the EBs have downward flows of about 0.1 to 0.3  $\text{km s}^{-1}$  at the photospheric level. In the low chromosphere, Kitai (1983) and Kurokawa *et al.* (1982) detected upflows with a speed of 6 to 8  $\text{km s}^{-1}$  from the far blue wings of the  $H\alpha$  line. In addition, transverse motions associated with EBs were observed in the photosphere (Jess *et al.*, 2010; Payne, 1993; Georgoulis *et al.*, 2002).

Some previous studies have reported that EBs were accompanied by surges (Altschuler, Lilliequist, and Nakagawa, 1968; Rust, 1968; Roy, 1973; Dara *et al.*, 1997; Matsumoto *et al.*, 2008; Watanabe *et al.*, 2011; Canfield, 1996). Matsumoto *et al.* (2008) found the ejection of  $H\alpha$ -absorbing material from an EB with a speed of 5  $\text{km s}^{-1}$  in the plane of the sky. Watanabe *et al.* (2011) also found similar events in images taken at several wavelengths of the  $H\alpha$  line with a Fabry-Perot interferometer. They examined 11 EBs and found that two of them were associated with surges. One of them initially appeared as an upflow with a line-of-sight (LOS) velocity of about 40  $\text{km s}^{-1}$ ; this EB later changed to a downflow. They occurred a few times during the observations.

Previous studies suggested that EBs occur in specific field configurations. Roy (1973) and Dara *et al.* (1997) showed that EBs are located near the boundaries of magnetic features. Georgoulis *et al.* (2002) showed that 70 % of the EBs were associated with bald-patch field lines, which represent magnetic dips of the U-loops in the photosphere, and the remaining 30 % of the EBs were associated with the quasi-separatrix layers in apparently monopole regions. This pattern was confirmed by other studies (Pariat, Aulanier, and Schmieder, 2004; Fang *et al.*, 2006; Pariat *et al.*, 2007).

It is now widely accepted that the driving mechanism of EBs is magnetic reconnection in the temperature-minimum region or in the low chromosphere (Pariat, Aulanier, and Schmieder, 2004; Georgoulis *et al.*, 2002; Pariat *et al.*, 2007; Isobe, Tripathi, and Archontis, 2007). Magnetic reconnection could explain the observed mass motions in the photosphere and chromosphere, including surges (Matsumoto *et al.*, 2008), a typical elongated shape of the inverse-Y shape (Watanabe *et al.*, 2011), and the local heating of the EBs with  $\Delta T \approx 500 - 2000$  K (Kitai, 1983; Fang *et al.*, 2006; Georgoulis *et al.*, 2002).

In this paper, we investigate the velocities and temperatures of plasmas of an EB and its associated features. We are interested in a variety of processes related to the same EB: the photospheric transverse motion and downflow at the site of the EB, the EB itself as a jet-like feature in the chromospheric level, and an intensely heated surge. The paper proceeds as follows. In Section 2 we introduce the observation and data processing. Section 3 contains the results, particularly on the velocity field inside the EB, the magnetic-field configuration around the EB, and the parameters of the EB-associated surge. Finally, we interpret and discuss our results in Section 4.

## 2. Observations and Data Processing

We observed a series of EBs near the pores in AR 11271 on 19 August 2011 using the Fast Imaging Solar Spectrograph (FISS) and a TiO broadband filter of the 1.6 m New Solar

Telescope at Big Bear Solar Observatory with the aid of adaptive optics. The FISS is an Echelle spectrograph that produces spatial and spectral information of the H $\alpha$  and Ca II 8542 Å lines simultaneously, using a fast scan of the slit across the field of view (Chae *et al.*, 2012). The spectral sampling is 19 mÅ in the H $\alpha$  line and 26 mÅ in the Ca II line, and the spectral coverage is 9.7 Å in the H $\alpha$  line and 12.9 Å in the Ca II line, which is broad enough to cover the lines. The region was located at 447'' eastward and 146'' northward of the disk center. The field of view (FOV) was 19.2'' in the scan direction and 40'' in the slit direction. The step size is 0.16'', which is the same as the sampling along the slit. The observation lasted for 2 h from 18:54:31 UT to 21:01:10 UT in steps of 20 s.

We performed basic processing of the FISS data – flat fielding, dark subtraction, and distortion correction – following Chae *et al.* (2012). The spatially averaged profiles of the H $\alpha$  line and Ti II 6559.580 Å photospheric line were used for the wavelength calibration of the H $\alpha$  band. With this calibration, the spatial average of the H $\alpha$  Doppler shift becomes zero. In the same way, the spatial averages of the Ca II line and Kr I 8537.93 Å line were used to calibrate the Ca II band. The measured standard error in the profile was 0.15 km s<sup>-1</sup> for H $\alpha$  and 0.21 km s<sup>-1</sup> for the Ca II line in the quiet region.

The region was observed with the TiO broadband filter as well, which is centered at a wavelength of 7057 Å and has a band width of 10 Å (Cao *et al.*, 2010). The best 70 images of the 100 short-exposure (1.2 ms) images in each burst were saved during the observation. After the dark subtraction and flat fielding, we applied the Kiepenheuer-Institut Speckle Interferometry Package (Wöger, von der Lühe, and Reardon, 2008) code to each burst. The FOV of the speckle-reconstructed images was 69.8'' × 69.8''. Bursts of images were taken repeatedly and the interval between two successive bursts was about 15 s.

Figure 1 shows a few raster images of the observed region constructed from the FISS data at several wavelengths and a speckle-reconstructed image through the TiO broadband filter. The spatial resolution of the FISS images is poorer than that of the TiO image partly because the initial focusing of the FISS was not set to the best focus (Chae *et al.*, 2012) and the atmospheric seeing was not as well corrected by the current adaptive optics as it is now.

The EB of our interest is clearly identified in the 6562.8 Å + 1.4 Å image. It is located at 437'' eastward and 146'' northward of the disk center, about 10'' away from the pores. The angle between the LOS and the radial direction,  $\mu$ , is about 30°. The surge appeared at the side of the EB and seems to have originated from it (see the H $\alpha$  and Ca II line center images of Figure 1). In the TiO filter image, we see many tiny bright points corresponding to the footpoints of magnetic flux tubes on the boundaries of granules.

### 3. Results

We observed three EBs and two surges during 2 h of observations. Our analysis is focused on the second EB and its associated surge because the data quality is better than the others. This event first appeared at 19:26:49 UT, which is taken to be the epoch of time  $t$ . Before the EB occurred, an oval-shaped granular cell expanded in the TiO photospheric images. When the lane of the granular cell reached the magnetic neutral line, the expansion stopped. Then the EB brightened and persisted for about 10 min. About 260 s after the EB brightening, we observed that the surge was ejected next to the EB.

The dataset of the first and third EBs is incomplete because of the poor atmospheric conditions. The third EB appeared at  $t = 820$  s. We found transverse motions in the TiO images before the brightening. Another surge was observed in the blue wing of the H $\alpha$  and Ca II lines at  $t = 920$  s.

In the next section, we explain the events related to the second EB in detail.

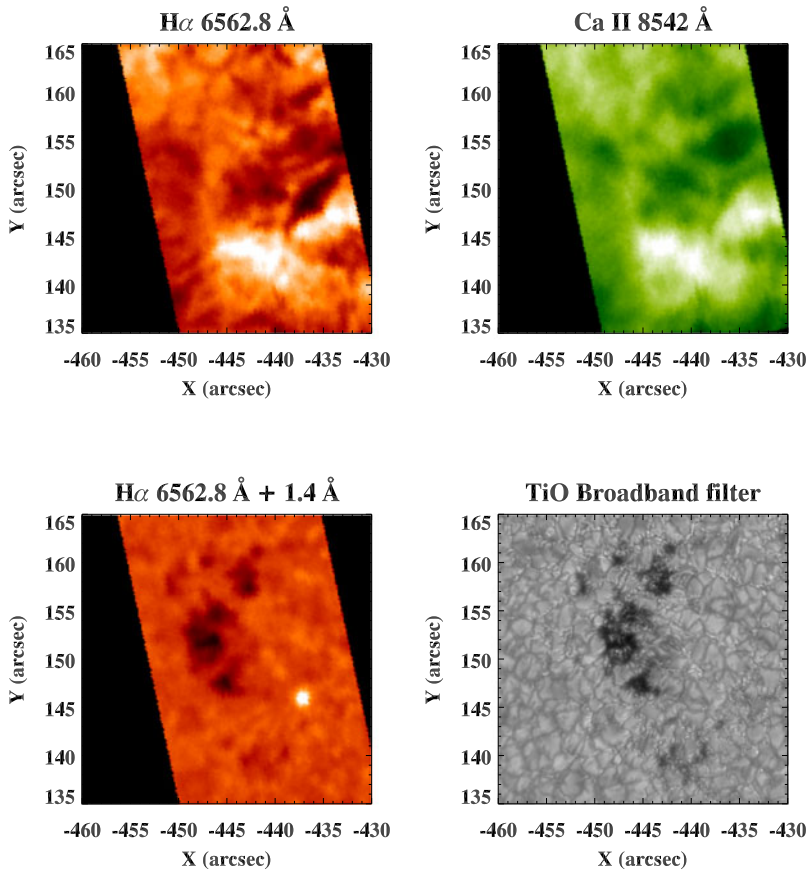


**Figure 1** The raster images of the H $\alpha$  line center (top left), the Ca II 8542 Å line center (top right), and the off-band (bottom left) of the FISS and TiO broadband filter image (bottom right) at 19:32:48 UT, 359 s after the occurrence of the EB.

### 3.1. Expanding Granular Cell

We found an oval-shaped granular cell expanding in two opposite directions near the site of the EB (see Figure 2). During this expansion period from  $-800$  s to  $200$  s, new dark lanes emerged inside the cell, which caused the cell to split into four sub-cells. One end of this expanding granule, surrounded by the dark lanes, reached the site where the EB occurred. As this approached the EB region, a small sub-cell appeared at the tip of this lane and then brightened. A set of 45-s cadence magnetograms of the *Helioseismic and Magnetic Imager* (HMI; Schou *et al.*, 2012) onboard the *Solar Dynamics Observatory* (SDO) suggests that the EB was located above the region where the magnetic flux gradient was steep. A weak positive-polarity region approached the EB site together with the expanding granule. At the other side of the granular cell, the steep-gradient magnetic polarity region also moved together with the expanding granule.

We measured the transverse speed,  $v_{\text{TiO}}$ , of the edge of the expanding granule in the direction toward the EB using the nonlinear affine velocity estimator (NAVE; Chae and Sakurai, 2008). We chose  $13 \times 13$  pixels in the TiO image as the window size, similar to the

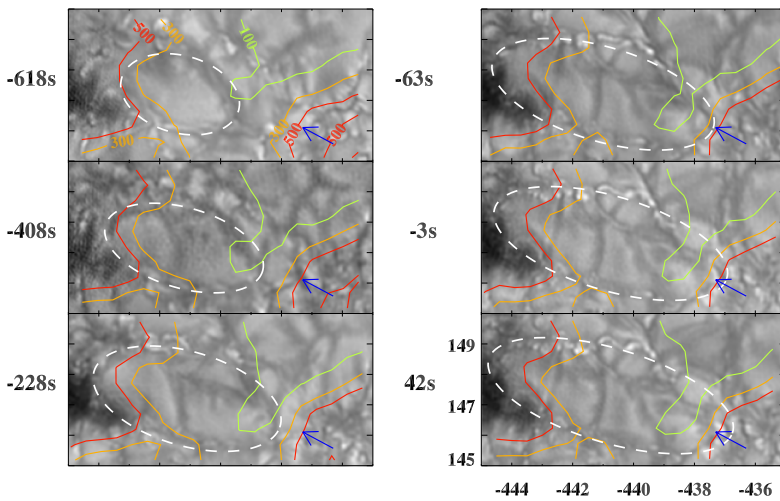


**Figure 2** Time series of TiO 7057 Å filter images. The blue arrows indicate the position of the EB. The time after the occurrence of the EB is presented at each image. White dashed ovals indicate the expanding granular cell of interest. The solid curves represent the levels of the vertical magnetic field in the HMI magnetograms.

size of the small sub-cell ( $0.5''$ ) that appeared at the tip of the lane. As a result, we found that  $v_{\text{TiO}}$  increased from  $1 \text{ km s}^{-1}$  up to  $5.5 \text{ km s}^{-1}$  in 350 s (see Figure 10(d)); this is three times faster than the typical granular flow speed, implying that this motion was not driven by photospheric granulation. After reaching its peak, the speed rapidly decreased to about  $1 \text{ km s}^{-1}$  within 100 s.

### 3.2. Photospheric Doppler Velocity

The LOS velocities in the photosphere of the EB were inferred from the photospheric line at  $6559.580 \text{ Å}$  in the  $\text{H}\alpha$ -band spectra by fitting a Gaussian profile to the line. The measured velocities looked somewhat noisy partly because the line is weak and they are subject to solar oscillation. Despite these problems, we found a persistent downflow of about  $1 \text{ km s}^{-1}$  at the EB location. The downflow started at  $-100 \text{ s}$ , and lasted for about 300 s. This value is larger than the standard error of  $0.11 \text{ km s}^{-1}$ .

### 3.3. Spectral Characteristics of the EB

Figure 3 shows the spectral characteristics of the EB seen in the  $\text{H}\alpha$  and Ca II line profiles. As is well known, the  $\text{H}\alpha$  line profile displays a broad emission profile at the wings and a narrow absorption at the center. The intensity monotonically increases in the emission wings as the wavelength approaches the line center and peaks at around  $\pm 1.0 \text{ Å}$ . The Ca II line profile of the EB appears in emission at every wavelength when compared with the reference profile of the surrounding area. Unlike the  $\text{H}\alpha$  profile, the intensity of the Ca II line decreases as the wavelength approaches the line center from the wings.

The intensity variation over wavelength at the wings reflects the height variation of the source function in the radiative transfer. The wings of the Ca II profile originate from the photosphere where local thermodynamic equilibrium (LTE) holds fairly well. The brightness temperature  $T_{\text{B}}$  of the photosphere where the EB is observed can be identified with the

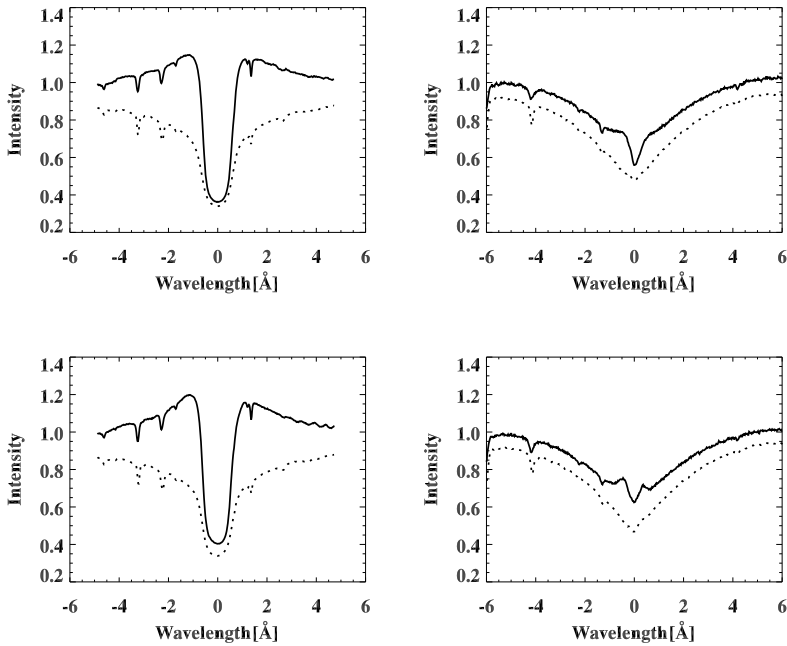


**Figure 3** The intensity profiles of the H $\alpha$  line (left) and the Ca II line (right) of the EB taken at 199 s (top) and 319 s (bottom) after the occurrence of EB. The solid lines represent the profile of the EB, and the dotted lines represent the reference profiles of the surrounding area.

temperature  $T$  of the formation region. Figure 3 hence indicates that the photosphere of the EB is characterized by the temperature excess  $\Delta T_B \approx 200$  K over the unperturbed one. This increase in the photospheric temperature is consistent with the brightening in the TiO images and with the brightening in the SDO/AIA 1600 Å and 1700 Å images that took place simultaneously with those of the H $\alpha$  and Ca II lines.

The H $\alpha$  profile of the EB itself is decomposed into a few components: central absorption, emission in the near wings, and “power-law emission in the far wings” (Kitai, 1983). We inferred the LOS velocity of the plasma responsible for the H $\alpha$  emission in the near wings,  $v_{\text{wing}}$ , with the lambdameter method. In this method,  $v_{\text{wing}}$  is determined from

$$v_{\text{wing}} = c \frac{\lambda_m - \lambda_0}{\lambda_0}, \tag{1}$$

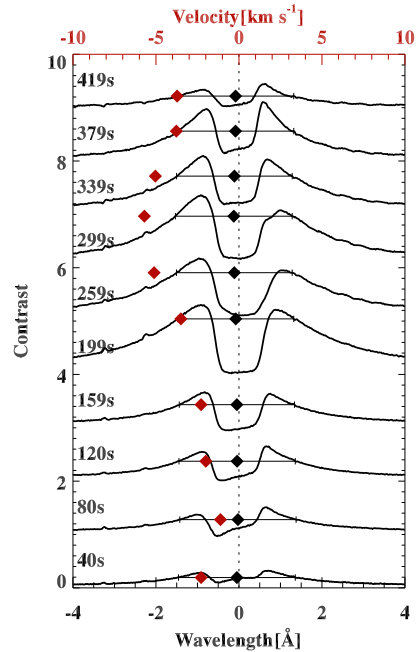
where  $\lambda_m$  is a measure of the Doppler shift and  $\lambda_0$  is the central wavelength of the line. The quantity  $\lambda_m$  is defined by

$$C\left(\lambda_m - \frac{\delta\lambda}{2}\right) = C\left(\lambda_m + \frac{\delta\lambda}{2}\right) = C_1, \tag{2}$$

where  $C(\lambda)$  is the contrast profile defined in Equation (3). The wavelength difference of the lambdameter,  $\delta\lambda$ , is set to 2.8 Å, which represents the emission characteristics well, and  $C_1$  is obtained as a by-product of the method. We applied this lambdameter method to the contrast profiles instead of to the spectral profiles because the characteristics of the EB may be better manifested in the contrast profiles.

Figure 4 shows the temporal variation of the contrast profiles of the EB. The emission wings of the EB lasted for about 500 s. During this period, they are blueshifted, and the

**Figure 4** Temporal variation of the H $\alpha$  contrast profiles of the EB. The contrast profiles are stacked vertically in the order of time. Black horizontal lines and diamond symbols represent the line widths of  $\delta\lambda$  (2.8 Å) and the values of  $\lambda_m$  of the emission wings. Red axis and red diamond symbols represent the calculated LOS velocities,  $v_{wing}$ .



resulting velocity  $v_{wing}$  gradually changed from 1 km s<sup>-1</sup> to 7 km s<sup>-1</sup> with an acceleration of 14 m s<sup>-2</sup>.

### 3.4. Surge

The raster images of the small region presented in Figure 5 show the second and third EBs and the surges associated with three EBs. The second EB is located at the bottom-left of every off-band raster image. After the second EB appeared, it brightened slowly with time and reached a peak at  $t = 298$  s, after which it darkened. The surge was visible from about  $t = 259$  s in the blue wings of the two lines. Later, the surge disappeared in the blue wings, but emerged in the red wings, indicating the gradual transition of the Doppler shift from blueshift to redshift.

Figure 6 shows the spectral profiles of the H $\alpha$  (left panel) and Ca II 8542 Å lines (right panel) taken from a spatial point inside the surge at  $t = 741$  s. The spectral profiles were normalized with respect to the far wings ( $|\lambda| > 2$  Å) of the Jungfrauoch atlas (Delbouille and Roland, 1995). The two contrast profiles appear in absorption and are redshifted. It is very likely that the observed surge was located high above the mean chromosphere. Thus, it could be considered to be similar to a cloud illuminated from below. To derive the physical parameters of the surge, we applied the classical cloud model of radiative transfer (Beckers, 1964). Note that the cloud model is applicable for the absorption feature. In this case, the surge can be analyzed using the model. According to the model, the contrast of the observed intensity profile  $I_\lambda^{out}$  against its background intensity profile  $I_\lambda^{in}$  is described as

$$C_\lambda \equiv \frac{I_\lambda^{out} - I_\lambda^{in}}{I_\lambda^{in}} = \left( \frac{S}{I_\lambda^{in}} - 1 \right) (1 - e^{-\tau_\lambda}), \tag{3}$$

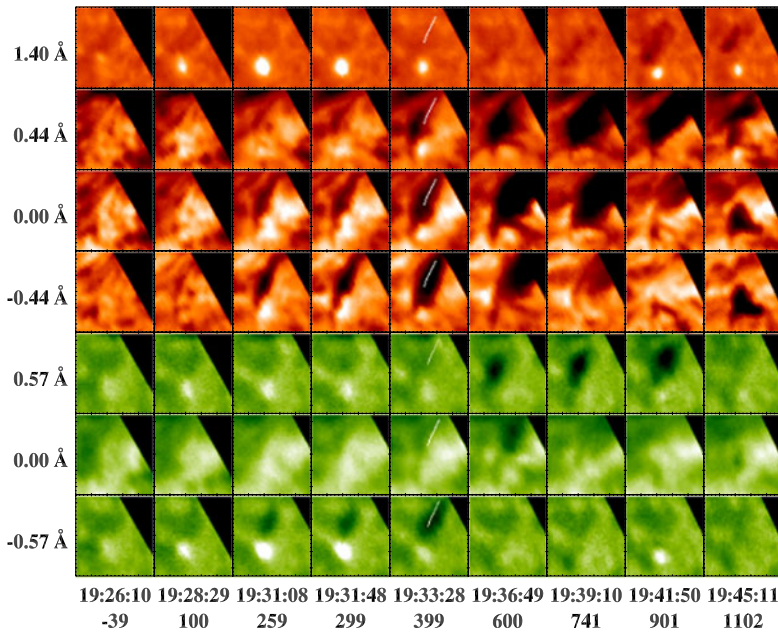


**Figure 5** The time sequence of the H $\alpha$  (top) and Ca II 8542 Å (bottom) lines in the red wing, center, and blue wing. The  $x$ -axis represents time in seconds from the first brightening of the EB. The field of view is  $10 \times 10''$ .

where  $S$  is the source function and  $\tau_\lambda$  is the optical depth. We adopted  $\tau_\lambda$  of the form

$$\tau_\lambda = \tau_{0,\lambda} \exp \left[ - \left( \frac{\lambda - \lambda_0}{\Delta\lambda_D} \right)^2 \right], \tag{4}$$

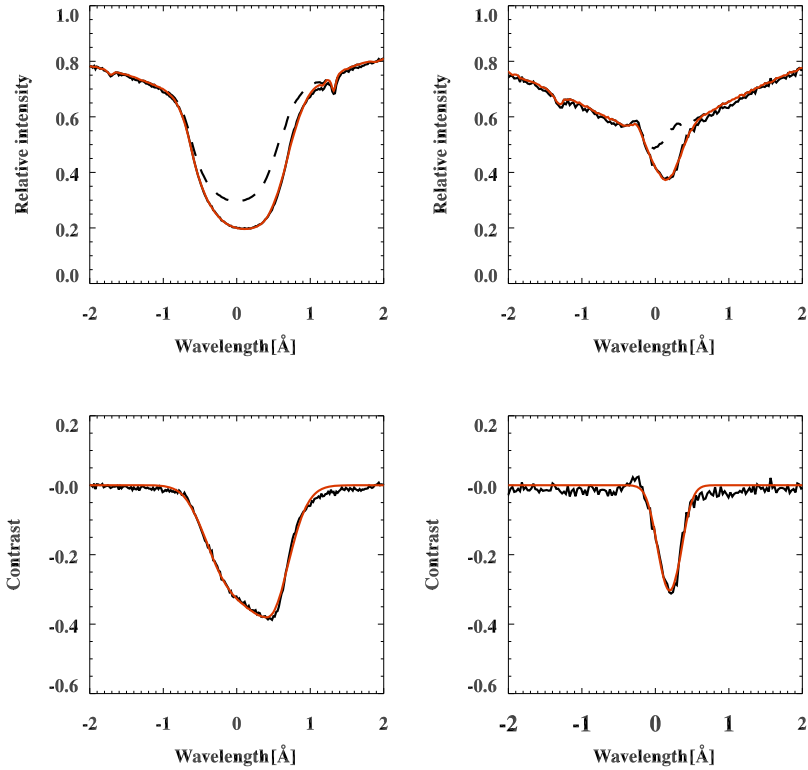
where  $\lambda_0$  is the central wavelength of the absorption profile,  $\Delta\lambda_D$  is the Doppler width of the line, and  $\tau_{0,\lambda}$  is the optical depth at the line center. Note that  $\lambda_0$  represents the LOS velocity  $v_0$ . The average over ten profiles taken at different times at the same location before the appearance of the surge was used for the background  $I_\lambda^{\text{in}}$ .

The cloud-model fitting was applied for the H $\alpha$  and Ca II lines. Then  $\lambda_0$ ,  $\tau_{0,\lambda}$ ,  $S$ , and  $\Delta\lambda_D$  were individually derived in two lines. The Doppler broadening  $\Delta\lambda_D$  contains the thermal contribution and the nonthermal contribution. Then  $\Delta\lambda_D$  is expressed as

$$\Delta\lambda_D = \frac{\lambda}{c} \sqrt{\frac{2kT}{M} + \xi^2}, \tag{5}$$

where,  $\lambda$ ,  $T$ ,  $M$ ,  $\xi$  are the wavelength at rest, the kinetic temperature, the mass of the atom, and the speed of the nonthermal motion (traditionally called microturbulence), respectively. If the H $\alpha$  and Ca II lines form in the same material, we can separately determine the values of  $T$  and  $\xi$  in the region from the two  $\Delta\lambda_D$ -values of the lines because the mass of the H I atom is different from that of the Ca II ion.

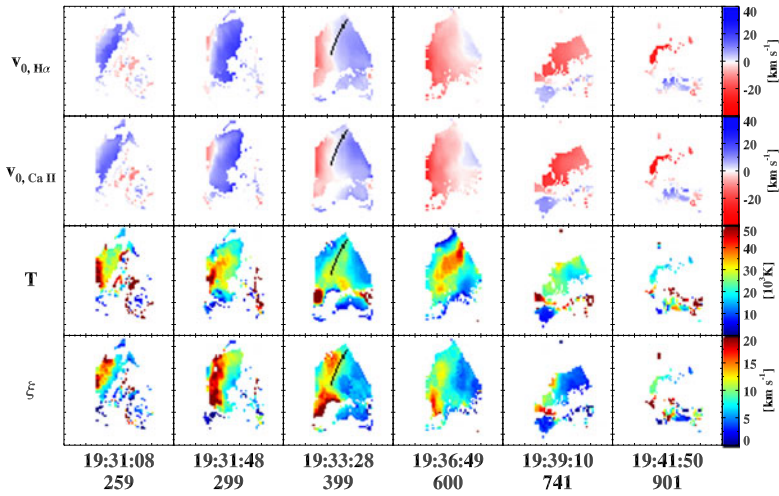
Figure 6 shows that the two profiles are fairly well fitted by the model. We find that the H $\alpha$  contrast profile has a higher absorption contrast and broader width than the Ca II profile. Nevertheless, they have similar LOS velocity (about  $6.8 \text{ km s}^{-1}$ ), which strongly supports our expectation that the two contrast profiles originate from the same material.



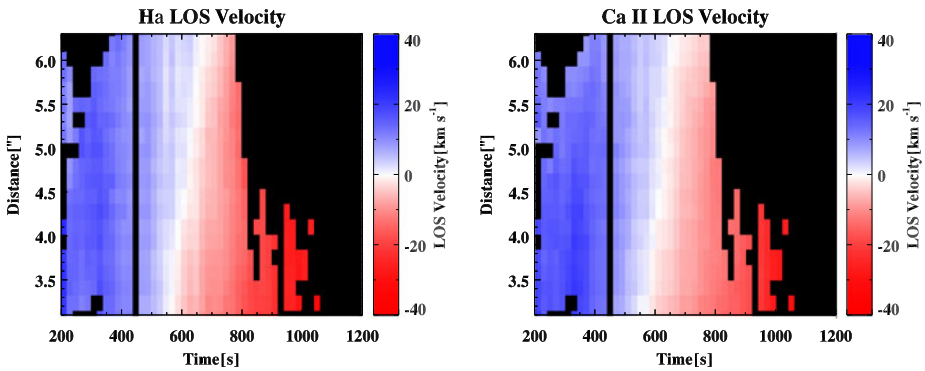
**Figure 6** The intensity (top) and contrast (bottom) profiles of the surge in the H $\alpha$  (left) and Ca II 8542 Å lines (right) at  $t = 741$  s. The black dashed lines represent the intensity profiles of the background radiation ( $I_{\lambda}^{\text{in}}$ ), and the black solid lines are the data. The red solid lines are the cloud-model fitting results. The obtained LOS velocities for the H $\alpha$  and the Ca II lines are  $v_{\text{H}\alpha} = 6.93 \text{ km s}^{-1}$ , and  $v_{\text{Ca II}} = 6.79 \text{ km s}^{-1}$ , respectively. The temperature and the nonthermal velocity are 24 700 K and  $6.72 \text{ km s}^{-1}$ , respectively.

Figure 7 shows the time-sequence maps of the LOS velocities  $T$  and  $\xi$  in each data set at the same FOV as shown in Figure 5. We manually masked the area of the surge by examining the images. After applying the fitting to the pixels inside the masked area, we discarded the points where the velocity difference between the H $\alpha$  and Ca II lines was bigger than  $5 \text{ km s}^{-1}$ . As shown in the figure, the surge was obviously blueshifted in the early phase, then it changed to the redshift. H $\alpha$  and Ca II lines show the same LOS velocities. The LOS velocity started to vary in the eastern part of the surge first, while the western part of the surge followed the variation. At the early phase of the surge, temperature  $T$  near the EB seems to be higher than the other part. Later,  $T$  at the middle of the surge increased to about 40 000 K. The value of  $\xi$  was higher than  $15 \text{ km s}^{-1}$  initially, but it decreased to about  $5 \text{ km s}^{-1}$  later.

We examined the temporal variation of physical parameters at 20 positions (about  $3.6''$ ) on the white curve marked in Figure 5. This curve follows the direction of the surge. At every position, we analyzed 50 profiles taken at different times during  $t = 200 \text{ s} - 1200 \text{ s}$ . Figure 8 shows the time-slice maps of the LOS velocities of the surge determined along the curve. We displayed values only at positions where the velocity difference between the H $\alpha$  and Ca II lines was smaller than  $5 \text{ km s}^{-1}$ . The correlation between the chosen values of



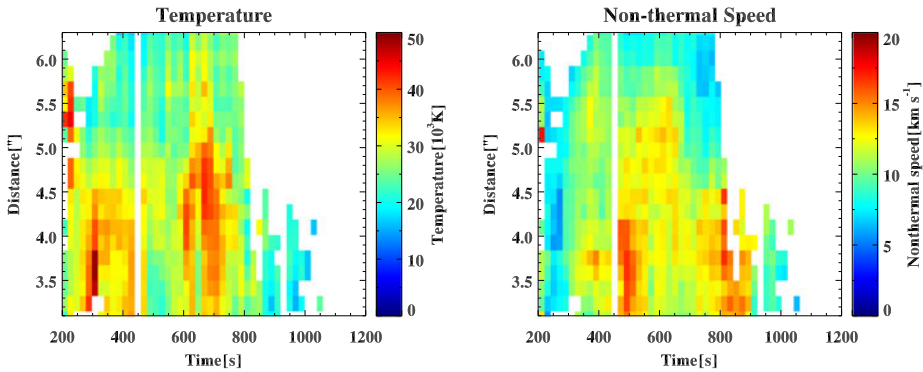
**Figure 7** The time-sequence maps of the LOS velocities of H $\alpha$  and Ca II 8542 Å lines, temperature and nonthermal velocity. The FOV is the same as in Figure 5.



**Figure 8** The time-slice maps of the LOS velocity of the surge calculated using the non-linear square fitting of the cloud model, in the H $\alpha$  (left panel) and Ca II 8542 Å (right panel) lines. The positive value represents the upward motion.

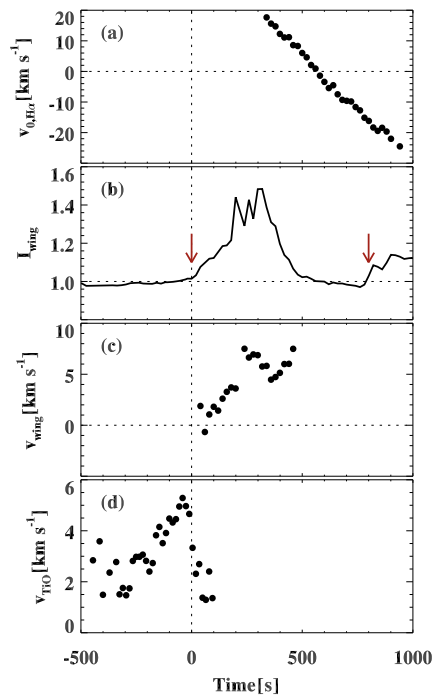
H $\alpha$  and Ca II is 0.99, and the standard deviation of  $v_{H\alpha} - v_{Ca II}$  is  $1.4 \text{ km s}^{-1}$ . The velocity at  $t = 200 \text{ s}$  was about  $20 \text{ km s}^{-1}$  upward. This blueshift simultaneously appeared at all positions, then they gradually changed and became redshifted. The estimated acceleration was almost constant ( $\approx -70 \text{ m s}^{-2}$  downward) during the event, which is much smaller than the free-fall acceleration ( $-274 \text{ m s}^{-2}$ ) on the solar surface.

Figure 9 shows that the distributions of  $T$  and  $\xi$  vary over time. As seen in the figure,  $T$  ranged from 20 000 K to 40 000 K, and  $\xi$  from  $5 \text{ km s}^{-1}$  to  $15 \text{ km s}^{-1}$ . The mean and  $1-\sigma$  values were found to be around  $29000 \pm 4700 \text{ K}$  and  $11.2 \pm 1.9 \text{ km s}^{-1}$ , respectively. Higher  $T$  values are found near the middle of the surge and higher  $\xi$  near its bottom. We found that  $T$  and  $\xi$  are moderately anti-correlated with a coefficient of  $-0.46$  near the EB. Furthermore, we found a tendency for  $T$  to be as high as 40 000 K before  $t = 800 \text{ s}$ , and



**Figure 9** The time-slice maps of temperature (left panel) and nonthermal velocity (right panel) of the surge.

**Figure 10** Temporal variation of (a) the LOS velocity of the surge at  $3.1''$  distance from the EB, (b) the intensity at  $6562.8 - 1.4 \text{ \AA}$ , (c) LOS velocity of emission wings of the EB, and (d) the transverse velocity under the EB. The LOS velocity of the surge is measured at  $3.1''$  far from the EB. The transverse velocity is measured following the lane of the expanding granular cell. The red arrows in (b) represent the second and third EBs.



then  $T$  dropped to  $20\,000 \text{ K}$  later. We also found a similar tendency that  $\xi$  decreased from  $15 \text{ km s}^{-1}$  to  $5 \text{ km s}^{-1}$ .

### 3.5. Summary of the Time Variation

The time variations of the velocities as well as the EB brightness are shown in Figure 10. It is evident that the speed of the photospheric transverse motion ( $v_{TiO}$ ) steadily increased and then decreased in a short time. The time of the transition from acceleration to deceleration coincides with the beginning of the EB, suggesting that they were physically related. The low-chromosphere velocity measured from the emission wings ( $v_{wing}$ ) increased during the

EB event, with an indication of a superposed oscillatory pattern at around  $t = 400$  s. This is a little before the instant when the surge was first visible, moving at a high speed of about  $20 \text{ km s}^{-1}$ . The LOS velocity of the surge ( $v_{0, \text{H}\alpha}$ ) monotonically decreased with an almost uniform deceleration of  $\approx 70 \text{ m s}^{-2}$ .

#### 4. Discussion

We have measured different kinds of velocity fields in relation to the EB as a function of time: the downflow and the transverse motion at the photospheric level, the upflow in the chromosphere, and the surge in the upper chromosphere or in the low corona. Moreover, we have obtained some results related to the heating process of the EB. We observed a brightening in the TiO images at the location of the EB. The intensity enhancement of the wings of the Ca II line indicates that the EB had a temperature excess of 200 K in the photosphere. The average temperature of the surge that originated from the EB was estimated to be about 29 000 K.

Our results help us to infer a comprehensive and detailed picture of various phenomena associated with the EB in the widely accepted frame of magnetic reconnection. In the photosphere, we observed events of brightening and downflow at the time of EB, and we also observed the upflow in the chromosphere. It is likely that these resulted from the magnetic reconnection that was responsible for the EB. If so, our observations suggest that the magnetic reconnection occurred between the upflow and the downflow regions – probably right above the photosphere, in agreement with previous studies (Georgoulis *et al.*, 2002; Pariat, Aulanier, and Schmieder, 2004; Watanabe *et al.*, 2011).

The observed magnetograms suggest that a magnetic bipole existed across the granular cell, even though the negative polarity was buried in the background positive pole (the resolution of the HMI is  $0.91''$  (Schou *et al.*, 2012)), and expanded together with the cell (see Figure 2). Therefore, the transverse bi-directional motions of the lanes might represent an emerging bipole, and the ends of the expanding granule might be the footpoints of the bipole. It is very likely that the EB was located above the photospheric magnetic neutral line and was driven by the collision of the emerging negative flux with the pre-existing positive flux. The event looks similar to the emergence of an  $\Omega$ -shaped flux loop observed by Lim *et al.* (2011).

Our observations indicate the driving force of the reconnection: it could be a small-scale flux emergence that manifested itself in an expanding granule. One end point of the granule – supposedly one footpoint of the emerging field – moved at a fast speed and eventually reached a point that was very close to the EB site, suggesting that the reconnection process responsible for this EB may have been driven by this flux emergence. The small distance between the end point of the granule and the EB site also suggests that the reconnection occurred at a low altitude. The observed motion toward the site of the EB was as fast as  $6 \text{ km s}^{-1}$  and hence is quite different from the previously reported continuous, wide horizontal flows with a speed of  $0.1\text{--}0.3 \text{ km s}^{-1}$  that were suspected to be inflows to the EB site (Georgoulis *et al.*, 2002). Rapidly converging flows of  $4\text{--}6 \text{ km s}^{-1}$  have been observed in recent high spatial resolution observations (Jess *et al.*, 2010; Lim *et al.*, 2011; Chae *et al.*, 2010). It is surprising that the speeds are as fast as the sound speed of the photospheric level. The transverse motion changed from acceleration to deceleration when the one end point of the granule reached the EB site. This rapid change may result from the high magnetic pressure of the flux pile-up site, which resists against further convergence of the magnetic elements and frozen-in plasma. At any rate, the fact that the EB started after the

end point of the granule reached the site strongly suggests that the transverse motion may have driven the process of magnetic reconnection, even though flux emergence is not seen in our data.

We also found a systematic difference in the profile shape of the EB between the  $H\alpha$  line and Ca II line. Unlike the  $H\alpha$  line, the spectral characteristics of the broad wing emission are not clear in Ca II. The Ca II 8542 Å line is strongly affected by the collisional effect because the line shares the upper level with the collisionally excited line, and hence reflects the temperature of the line formation region. In contrast, the  $H\alpha$  line is dominated by radiative processes such as radiative excitation/de-excitation and photoionization/radiative recombination, and hence is insensitive to the local kinetic temperature in the chromosphere (Cauzzi *et al.*, 2009; Chae *et al.*, 2012). Therefore, the above spectral characteristics strongly suggest that the broad emission wings of the  $H\alpha$  line in the EB may have a nonthermal origin, possibly an energetic-particle beam (Ding, Henoux, and Fang, 1998).

Even though we were unable to resolve the EB in our observations, recent high-resolution observations such as reported by Watanabe *et al.* (2011) indicate that the EB has a shape of an anemone jet. The speeds of the upflow in the EB we observed and those of previous measurements (Kitai, 1983; Kurokawa *et al.*, 1982) are consistent with this new picture. If the material moves upward for 500 s with the speed of  $1-7 \text{ km s}^{-1}$  as shown in Figure 10, it can reach a height of about 2500 m, which is higher than the typical EB size of  $1.8''$  (1300 km).

Our results may contribute to a better understanding of the dynamics and energetics of the surge that originates from the EB. Note that the surge had a speed of  $20 \text{ km s}^{-1}$  from the first instant when it emerged as a clear dark feature. The speed of the surge at the earlier times may have been even higher than this value because it was already decelerating at the instant of the observation. Choosing  $\Delta t = 200 \text{ s}$  for the duration of the initial acceleration, and  $v = 25 \text{ km s}^{-1}$  for the peak speed, we obtained  $-125 \text{ m s}^{-2}$  as an estimate of the average deceleration. The temperature and speed of the surge we obtained appear to be consistent with the observation of Tziotziou, Tsiropoula, and Sütterlin (2005), which yielded a temperature of  $10^4 - 10^5 \text{ K}$ , and the simulation of Yokoyama and Shibata (1996), which yielded a speed of a few tens of  $\text{km s}^{-1}$ .

Our finding that the surge has temperatures ranging from 20 000 to 40 000 K raises an important question to be addressed; how can the surge at such high temperatures be seen in the  $H\alpha$  and Ca II absorption? First, why in absorption, not in emission? This is because the scattering process dominates in the source functions of the lines in the low-density, high-lying features. Temperature is not that important in this system governed by scattering processes. Second, how can neutral hydrogen exists at such high temperatures? This is a serious problem. It is well-known that in LTE, most hydrogen atoms are ionized at temperatures above 20 000 K. This behavior appears to hold even in non-LTE because we find that temperatures inside filaments/prominences are measured to be lower than 20 000 K (Park *et al.*, 2013; Song, Henoux, and Fang, 2013). One possible explanation for this discrepancy is that the surge material may not be in ionization equilibrium. This kind of deviation from equilibrium arises when the ionization/recombination timescales ( $10^3 - 10^5 \text{ s}$  in the chromosphere according to Carlsson and Stein (2002)) are longer than the dynamic timescales, such as in the surge in which the dynamic timescale is a few hundred seconds, as we observed.

In conclusion, our observations support the picture that an EB and its associated surge is a response of the atmosphere to the process of magnetic reconnection that is driven by small-scale flux emergence and occurs in the low chromosphere.

**Acknowledgements** We greatly appreciate the referee's constructive comments. We are grateful to the BBSO team for their technical support for the observations. This work was supported by the National Research Foundation of Korea (2011-0028102). E.-K. Lim is supported by the "Study of near-Earth effects

by CME/HSS” project and basic research funding from KASI. Yeon-Han Kim and Eun-Kyung Lim were supported by the Construction of Korean Space Weather Center, the project of KASI, and the KASI basic research fund.

## References

- Altschuler, M.D., Lilliequist, C.G., Nakagawa, Y.: 1968, A possible acceleration mechanism for a solar surge. *Solar Phys.* **5**, 366–376. doi:[10.1007/BF00147150](https://doi.org/10.1007/BF00147150).
- Beckers, J.M.: 1964, A study of the fine structures in the solar chromosphere. Ph.D. thesis, Sacramento Peak Observatory, Air Force Cambridge Research Laboratories, USA.
- Canfield, R.: 1996, H $\alpha$  surges and X-ray jets in AR 7260. *Astrophys. J.* **464**, 1016–1029. doi:[10.1086/7389](https://doi.org/10.1086/7389).
- Cao, W., Gorceix, N., Coulter, R., Ahn, K., Rimmele, T.R., Goode, P.R.: 2010, Scientific instrumentation for the 1.6 m New Solar Telescope in Big Bear. *Astron. Nachr.* **331**. doi:[10.1002/asna.201011390](https://doi.org/10.1002/asna.201011390).
- Carlsson, M., Stein, R.F.: 2002, Dynamic hydrogen ionization. *Astrophys. J.* **572**, 626–635. doi:[10.1086/340293](https://doi.org/10.1086/340293).
- Cauzzi, G., Reardon, K., Rutten, R.J., Tritschler, A., Uitenbroek, H.: 2009, The solar chromosphere at high resolution with IBIS. IV. Dual-line evidence of heating in chromospheric network. *Astron. Astrophys.* **503**, 577–587. doi:[10.1051/0004-6361/200811595](https://doi.org/10.1051/0004-6361/200811595).
- Chae, J., Sakurai, T.: 2008, A test of three optical flow techniques – LCT, DAVE, and NAVÉ. *Astrophys. J.* **689**, 593–612. doi:[10.1086/592761](https://doi.org/10.1086/592761).
- Chae, J., Goode, P.R., Ahn, K., Yurchyshyn, V., Abramenko, V., Andic, A., Cao, W., Park, Y.D.: 2010, New Solar Telescope observations of magnetic reconnection occurring in the chromosphere of the quiet Sun. *Astrophys. J. Lett.* **713**, L6–L10. doi:[10.1088/2041-8205/713/1/L6](https://doi.org/10.1088/2041-8205/713/1/L6).
- Chae, J., Park, H.-M., Ahn, K., Yang, H., Park, Y.-D., Nah, J., Jang, B.H., Cho, K.-S., Cao, W., Goode, P.R.: 2012, Fast Imaging Solar Spectrograph of the 1.6 meter New Solar Telescope at Big Bear Solar Observatory. *Solar Phys.* doi:[10.1007/s11207-012-0147-x](https://doi.org/10.1007/s11207-012-0147-x).
- Dara, H.C., Alissandrakis, C.E., Zachariadis, T.G., Georgakilas, A.A.: 1997, Magnetic and velocity field in association with Ellerman bombs. *Astron. Astrophys.* **322**, 653–658.
- Delbouille, L., Roland, G.: 1995, High-resolution solar and atmospheric spectroscopy from the Jungfraujoeh high-altitude station. *Opt. Eng.* **34**, 2736–2739. doi:[10.1117/12.205676](https://doi.org/10.1117/12.205676).
- Ding, M.D., Henoux, J.-C., Fang, C.: 1998, Line profiles in moustaches produced by an impacting energetic particle beam. *Astron. Astrophys.* **332**, 761–766.
- Ellerman, F.: 1917, Solar hydrogen “bombs”. *Astrophys. J.* **46**, 298–300. doi:[10.1086/142366](https://doi.org/10.1086/142366).
- Fang, C., Tang, Y.H., Xu, Z., Ding, M.D., Chen, P.F.: 2006, Spectral analysis of Ellerman bombs. *Astrophys. J.* **643**, 1325–1336. doi:[10.1086/501342](https://doi.org/10.1086/501342).
- Georgoulis, M.K., Rust, D.M., Bernasconi, P.N., Schmieder, B.: 2002, Statistics, morphology, and energetics of Ellerman bombs. *Astrophys. J.* **575**, 506–528. doi:[10.1086/341195](https://doi.org/10.1086/341195).
- Isobe, H., Tripathi, D., Archontis, V.: 2007, Ellerman bombs and jets associated with resistive flux emergence. *Astrophys. J. Lett.* **657**, L53–L56. doi:[10.1086/512969](https://doi.org/10.1086/512969).
- Jess, D.B., Mathioudakis, M., Browning, P.K., Crockett, P.J., Keenan, F.P.: 2010, Microflare activity driven by forced magnetic reconnection. *Astrophys. J. Lett.* **712**, L111–L115. doi:[10.1088/2041-8205/712/1/L111](https://doi.org/10.1088/2041-8205/712/1/L111).
- Kitai, R.: 1983, On the mass motions and the atmospheric states of moustaches. *Solar Phys.* **87**, 135–154. doi:[10.1007/BF00151165](https://doi.org/10.1007/BF00151165).
- Kurokawa, H., Kawaguchi, I., Funakoshi, Y., Nakai, Y.: 1982, Morphological and evolutionary features of Ellerman bombs. *Solar Phys.* **79**, 77–84. doi:[10.1007/BF00146974](https://doi.org/10.1007/BF00146974).
- Lim, E.-K., Yurchyshyn, V., Abramenko, V., Ahn, K., Cao, W., Goode, P.: 2011, Photospheric signatures of granular-scale flux emergence and cancellation at the penumbral boundary. *Astrophys. J.* **740**, 82. doi:[10.1088/0004-637X/740/2/82](https://doi.org/10.1088/0004-637X/740/2/82).
- Matsumoto, T., Kitai, R., Shibata, K., Otsuji, K., Naruse, T., Shiota, D., Takasaki, H.: 2008, Height dependence of gas flows in an Ellerman bomb. *Publ. Astron. Soc. Japan* **60**, 95–102.
- Pariat, E., Aulanier, G., Schmieder, B.: 2004, Resistive emergence of undulatory flux tubes. *Astrophys. J.* **614**, 1099–1112. doi:[10.1086/423891](https://doi.org/10.1086/423891).
- Pariat, E., Schmieder, B., Berlicki, A., Deng, Y., Mein, N., Ariste, A.L., Wang, S.: 2007, Spectrophotometric analysis of Ellerman bombs in the Ca II, H $\alpha$ , and UV range. *Astron. Astrophys.* **289**, 279–289. doi:[10.1051/0004-6361:20067011](https://doi.org/10.1051/0004-6361:20067011).

- Park, H., Chae, J., Song, D., Maurya, R., Yang, H., Park, Y., Jang, B., Nah, J., Cho, K., Kim, Y., Ahn, K., Cao, W., Goode, P.: 2013, Determination of temperature of solar prominences/filaments using Fast Imaging Solar Spectrograph with the 1.6 m New Solar Telescope at the Big Bear Solar Observatory – I. Limb. *Solar Phys.* doi:[10.1007/s11207-013-0271-2](https://doi.org/10.1007/s11207-013-0271-2).
- Payne, T.E.W.: 1993, A multiwavelength study of solar Ellerman bombs. Ph.D. thesis, New Mexico State University.
- Roy, J.R.: 1973, The magnetic properties of solar surges. *Solar Phys.* **28**, 95–114. doi:[10.1007/BF00152915](https://doi.org/10.1007/BF00152915).
- Rust, D.: 1968, Chromospheric explosions and satellite sunspots In: Kiepenheuer, K.O. (ed.) *Structure and Development of Solar Active Regions, IAU Symp.* **35**, 77–84.
- Schou, J., Scherrer, P.H., Bush, R.I., Wachter, R., Couvidat, S., Rabello-Soares, M.C., Bogart, R.S., Hoeksema, J.T., Liu, Y., Duvall, T.L., Akin, D.J., Allard, B.A., Miles, J.W., Rairden, R., Shine, R.A., Tarbell, T.D., Title, A.M., Wolfson, C.J., Elmore, D.F., Norton, A.A., Tomczyk, S.: 2012, Design and ground calibration of the Helioseismic and Magnetic Imager (HMI) instrument on the Solar Dynamics Observatory (SDO). *Solar Phys.* **275**, 229–259. doi:[10.1007/s11207-011-9842-2](https://doi.org/10.1007/s11207-011-9842-2).
- Song, D., Henoux, J.-C., Fang, C.: 2013, Determination of temperature of solar prominences/filaments using Fast Imaging Solar Spectrograph with the 1.6 m New Solar Telescope at the Big Bear Solar Observatory – II. Filament. *Solar Phys.* submitted.
- Tziotziou, K., Tsiropoula, G., Sütterlin, P.: 2005, DOT tomography of the solar atmosphere. V. Analysis of a surge from AR10486. *Astron. Astrophys.* **444**, 265–274. doi:[10.1051/0004-6361:20053604](https://doi.org/10.1051/0004-6361:20053604).
- Watanabe, H., Vissers, G., Kitai, R., Voort, L.R.V.D., Rutten, R.J.: 2011, Ellerman bombs at high resolution: I. Morphological evidence for photospheric reconnection. *Astrophys. J.* **736**, 71. doi:[10.1088/0004-637X/736/1/71](https://doi.org/10.1088/0004-637X/736/1/71).
- Wöger, F., von der Lühe, O., Reardon, K.: 2008, Speckle interferometry with adaptive optics corrected solar data. *Astron. Astrophys.* **488**, 375–381. doi:[10.1051/0004-6361:200809894](https://doi.org/10.1051/0004-6361:200809894).
- Yokoyama, T., Shibata, K.: 1996, Numerical simulation of solar coronal X-ray jets based on the magnetic reconnection model. *Publ. Astron. Soc. Japan* **48**, 353–376.